Unconstrained Tree Tensor Network: An adaptive gauge picture for enhanced performance

M. Gerster,[1] P. Silvi,[1] M. Rizzi,[2] R. Fazio,[3,4] T. Calarco,[1] and S. Montangero[1]

[1] *Institut für Quanteninformationsverarbeitung, Universität Ulm, D-89069 Ulm, Germany*
[2] *Institut für Physik, Johannes-Gutenberg-Universitaet, D-55128 Mainz*
[3] *NEST, Scuola Normale Superiore & Istituto Nanoscienze CNR, I-56126 Pisa, Italy*
[4] *Centre for Quantum Technologies, National University of Singapore, 3 Science Drive 2, 117543 Singapore*

(Dated: March 1, 2022)

We introduce a variational algorithm to simulate quantum many-body states based on a tree tensor network ansatz which releases the isometry constraint usually imposed by the real-space renormalization coarse-graining: This additional numerical freedom, combined with the loop-free topology of the tree network, allows one to maximally exploit the internal gauge invariance of tensor networks, ultimately leading to a computationally flexible and efficient algorithm able to treat open and periodic boundary conditions on the same footing. We benchmark the novel approach against the 1D Ising model in transverse field with periodic boundary conditions and discuss the strategy to cope with the broken translational invariance generated by the network structure. We then perform investigations on a state-of-the-art problem, namely the bilinear-biquadratic model in the transition between dimer and ferromagnetic phases. Our results clearly display an exponentially diverging correlation length and thus support the most recent guesses on the peculiarity of the transition.

PACS numbers: 05.30.-d, 02.70.-c, 03.67.Mn, 05.50.+q

I. INTRODUCTION

Simulating quantum many-body states with tailored microscopical variational ansätze has been refreshed in the last decade thanks to the introduction of tensor network states. Despite being originally related[1–3] to density matrix renormalization group[4–6] schemes, these variational architectures have been engineered to encompass a wide variety of physical situations[7,8], thus widening the capabilities of the traditional numerical renormalization group (RG) approach. Generally, tensor networks encode in a compact, numerically efficient way, many-body wavefunction amplitudes over a real-space local basis expansion: the main reason for this real-space choice is the fact that, since typical Hamiltonians are characterized by two-body interactions which decay sufficiently fast with the pairwise distance, physically meaningful states (e.g. ground states, lowest excited states, thermal states) obey precise scaling laws on entanglement entropy under a real-space bipartition[9–12]. Such entanglement scaling can be precisely encoded in the tensor network paradigm[13,14] and led to the design of various tensor network geometries, such as Matrix Product States (MPS)[1], PEPS[15], Complete Graph states[16].

A physically sensible class of tensor network architectures are the hierarchical (or holographic[17]) tensor networks: they have the key feature of combining the usual local quantum space numerical renormalization together with a real-space coarse graining, much like in the original RG picture by Wilson[18]. Tree tensor networks (TTN)[19,20], multiscale entanglement renormalization ansatz (MERA) states[21–23], and the recently-introduced branching MERA[24], are the most prominent examples of hierarchical tensor networks. The fact that their network structure naturally embeds a scale invariance, makes them the ideal choice for representing critical (gapless) quantum phases of matter, which are characterized by conformal invariance[25]. Moreover, hierarchical tensor networks can indeed satisfy the scaling rules of entanglement of critical states[26], both in those cases where area laws are logarithmically violated (e.g. in 1D critical systems) and in those where area laws are satisfied (e.g. bosonic critical systems in two or higher dimensions)[14].

TTN states show a smooth computational scaling with the tensor network bond dimension m for the involved algebraic operations (e.g. for binary TTN it is never higher than $\mathcal{O}(m^4)$). This allows one to push numerical precision and description capabilities by sensitively increasing m, making the TTN ansatz a potentially competitive method for simulating quantum many-body states. On the other hand, TTN suffer more of a kind of entanglement clusterization, which is much more alleviated in other approaches, such as MERA, thanks to the presence of disentangling operations in their structure.

It is important to stress that the traditional scheme for simulating quantum lattice models with TTN states[27] relies on a particular selection of the internal tensor network gauge symmetry: in accordance to the RG flow picture by Wilson, the tensors are fixed to be isometric operators in the real-space renormalization direction. Although this gauge selection has indeed historical motivation, and moreover it guarantees some useful mathematical properties in the thermodynamical limit (namely, the complete positivity of the causal maps[20,21,23,28]), it confers no advantage in the simulation of finite-size systems, where actually it is more a hindrance. Instead, if no "a priori" rigid selection of the isometric gauge from bottom to top is made, one can always adjust the tensor network gauge to gain a computational enhancement in

the algorithm. This type of manipulation is particularly useful for tensor networks without closed loops in their topology, like TTN, for which gauge flexibility translates into a simplification of the variational algorithm into a simple eigenvalue problem (as it happens, for instance, for open boundary MPS compared to periodic ones).

In this manuscript we describe in detail an algorithm to find the ground state of quantum lattice Hamiltonians, based on unconstrained (i.e. gauge adaptive) tree tensor networks. We discuss thoroughly the computational cost scaling with numerical parameters, first of all the tensor network bond dimension m. We test the algorithm on one-dimensional quantum models, in both open (OBC) and periodic boundary conditions (PBC): we use the quantum Ising model as a benchmark, and then investigate the bilinear-biquadratic spin-1 model in proximity of the interface between the ferromagnetic and dimer phases. In the latter, a peculiar exponential scaling of correlation lengths has been conjectured to explain the traditional toughness of the numerical problem. The nice agreement of our data with the most recent state-of-the-art calculations corroborates the validity of the variational strategy presented here. We also address the problem of restoration of translational invariance, which is broken by the TTN architecture; we inquire for which physical quantities it is meaningful to average incoherently over translations as opposed to local evaluation over a highly-entangled cluster of sites. Ultimately, such investigation reveals quite a different behavior between local observations and correlations.

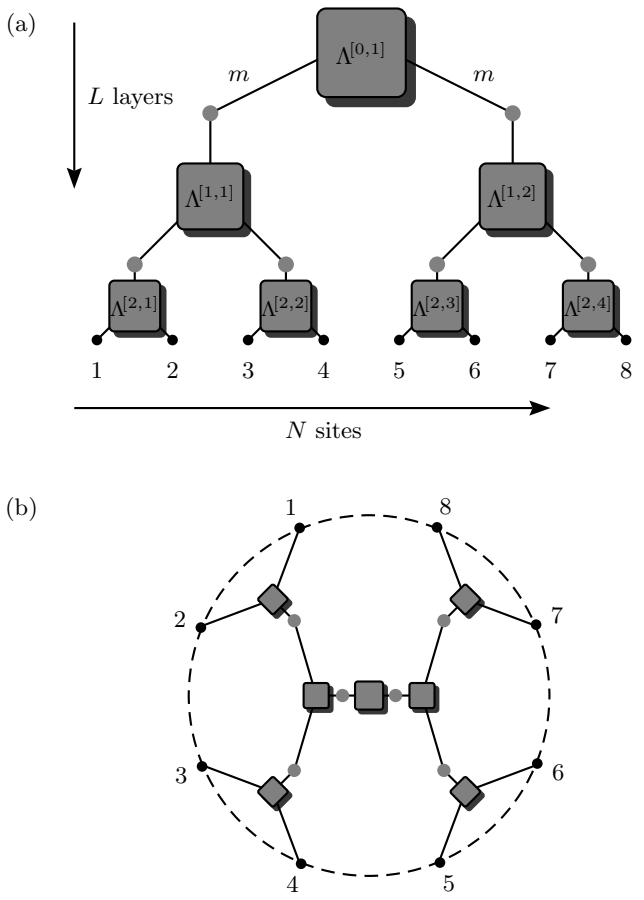

FIG. 1: (a) Structure of the binary TTN with L layers and N sites. The maximal bond dimension is m. (b) The same TTN displayed in a PBC configuration, showing its natural capability of treating OBC and PBC on the same footing.

II. STATE ARCHITECTURE AND ALGORITHM

We consider a one-dimensional lattice with $N = 2^L$ sites, where each site has a local Hilbert dimension of d. Our ansatz to approximate a many-body quantum state $|\Psi\rangle = \sum_{\{\vec{\chi}\}} \Psi_{\chi_1 \dots \chi_N} \bigotimes_{i=1}^{N} |\chi_i\rangle$ on such lattice, where the strings $\vec{\chi} = (\chi_1 \dots \chi_N)$ label the configurations of the N sites in some local "canonical" basis (with $\chi_i = 1 \dots d$), is displayed in Fig. 1: It is a binary TTN[19,20,27], a hierarchical structure consisting of L layers of tensors $\Lambda^{[l,n]}$ with three indices each, where $l = 0 \dots L-1$ indicates the layer and $n = 1 \dots 2^l$ denotes the horizontal position of the tensor. The sketch follows the usual convention of drawing tensor indices as "legs" or "links"; joining two tensor legs has the usual meaning of a contraction, i.e. a summation over the corresponding indices of the tensor elements product. All tensors in Fig. 1 have three legs, except for the top tensor $\Lambda^{[0,1]}$ which is two-legged: it can be viewed as the contraction of a three-legged tensor with a vector encompassing a wavefunction on a renormalized (degenerate) manifold[29]. The physical sites of the chain are represented by the dots attached to the bottom of the lowest layer of tensors. Each tensor effectively merges two sites into a single "virtual" site, allowing one to interpret the tensors as coarse-graining linear maps in a RG flow. Labeling the sites (either physical or virtual) with $[l,n]$ ($l = 1 \dots L$: layer coordinate, $n = 1 \dots 2^l$: horizontal coordinate), the tensor $\Lambda^{[l,n]}$ maps the two sites $[l+1, 2n-1]$ and $[l+1, 2n]$ to the site $[l,n]$. Consequently, the full Hilbert spaces of the sites in layer l have dimension $M(l) = d^{2^{L-l}}$. Such dimension is exponentially growing in the number 2^{L-l} of physical sites blocked together in layer l, and therefore a numerically efficient representation of such degrees of freedom requires some kind of space truncation. The most easily controlled truncation method is fixing a maximally allowed value m (an upper bound to the so-called "bond dimension"), resulting in $M(l) = \min(d^{2^{L-l}}, m)$. Moreover, the total number of tensors in the binary tree network is $N-1$, and since we are not introducing additional constraints in the variational picture, the total number of parameters in the TTN representation ultimately scales like $\mathcal{O}(N\, m^3)$.

In this manuscript, we are going to apply this variational ansatz to approximate the ground state of nearest-neighbor interacting spin-Hamiltonians on a lattice. The application to bosons is straightforward, while extension

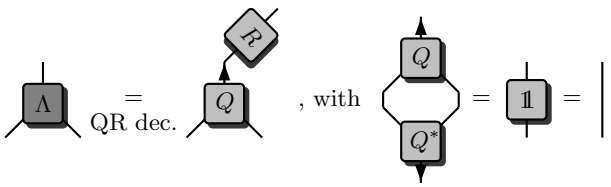

FIG. 2: Isometrization of a three-legged tensor Λ. The arrow indicates the leg with respect to which the tensor is isometric. In the picture, Q^* is the element-wise complex complex conjugate of Q, and it also drawn as vertically reflected.

to fermions is carried out via standard Jordan-Wigner transformation[30]. For convenience, we write the local fields and the spin-spin interactions separately, resulting in a Hamiltonian of the following form:

$$H = \sum_n \mathcal{H}^{[n]} + \sum_n \sum_\alpha \lambda_\alpha \, \mathcal{H}_{\leftarrow}^{\alpha[n]} \mathcal{H}_{\rightarrow}^{\alpha[n+1]} \,, \qquad (1)$$

where $\mathcal{H}^{[n]}$ (local term), $\mathcal{H}_{\leftarrow}^{[n]}$ (left interaction term) $\mathcal{H}_{\rightarrow}^{[n]}$ (right interaction term) are on-site operators acting on site n. The index α accounts for the fact that the interaction term can consist of several tensor-product contributions, weighted by their couplings λ_α. A strong point of the TTN ansatz is that it adapts comparatively well to both the OBC ($n = 1 \dots N-1$) setting and the PBC ($n = 1 \dots N$ and $N+1 \equiv 1$) setting. In the two cases, the computational costs are equal, and the numerical precisions compatible.

A key requirement for any tensor network representation is its efficient contractibility, which is instrumental to gain access to physically sensible information on the quantum many-body state, such as its energy or expectation values of observables. Indeed, a prominent advantage of TTN architectures is that they are algebraically contractible, thus providing exact expectation values efficiently, without the need of stochastic sampling of their variational data[31,32]. One can easily identify two properties of TTN that make this possible: The first is the loopless structure of the tree network and the second is the exploitation of a flexible, adaptive isometric gauge selection. The latter is based on a straightforward generalization of the QR-decomposition[33] applied to three-legged tensors Λ, which produces a directed-isometric tensor Q and a matrix R, such that

$$\Lambda_{\alpha_1\alpha_2\alpha_3} = Q_{\alpha_1\alpha_2\beta_1} R_{\beta_1\alpha_3} \,, \quad Q^*_{\alpha_1\alpha_2\beta_1} Q_{\alpha_1\alpha_2\beta_2} = \delta_{\beta_1\beta_2} \,, \qquad (2)$$

where Q is isometric with respect to the third leg (in the graphical notation of the TTN, we draw an outgoing arrow from Q on that leg). In Fig. 2 we report Eq. (2) expressed in graphical notation. We say that the TTN is isometrized with respect to tensor $\Lambda^{[l,n]}$ if all the other tensors in the tree are isometrized in the direction of this tensor according to the network structure, i.e. all the arrows are pointing towards $\Lambda^{[l,n]}$. Note that due to the loopless topology of the TTN such an isometric gauge

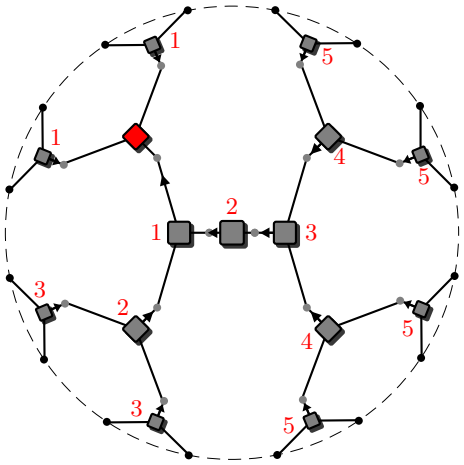

FIG. 3: TTN isometrization with respect to the tensor highlighted in red, i.e. all isometrization arrows point towards this tensor. To obtain this gauge, QR-decompose all tensors in order of decreasing distance (indicated by red numbers).

is always unique (apart from unitary gauge transformations) and efficiently attainable: just perform the QR-decomposition Eq. (2) for all the tensors, starting from the most distant ones (in the network metric, i.e. the graph distance of two nodes in the tree network) and absorbing the gauge matrices R into tensors yet to be isometrized, until reaching $\Lambda^{[l,n]}$. This concept is illustrated in Fig. 3. Also, note that in the adaptive isometric gauge the calculation of the many-body state norm $\langle\Psi|\Psi\rangle$ simply collapses to $\Lambda^{*[l,n]}_{\alpha_1\alpha_2\alpha_3}\Lambda^{[l,n]}_{\alpha_1\alpha_2\alpha_3}$ regardless of the node position in the network, since all the other partial contractions cancel to identities due to the isometry condition.

Such a flexible gauge selection provides a crucial advantage along the search for the best TTN representation of the ground state of the Hamiltonian H in Eq. (1). Expressed in a variational sense, the task consists in searching the set of tensors $\{\Lambda^{[l,n]}\}$ such that $E = \langle\Psi|H|\Psi\rangle/\langle\Psi|\Psi\rangle$ is minimal. For practical values of N and m the complete space of variational parameters of all tensors combined is too large to allow a successful application of a direct search optimization; instead, the approach pursued here relies on an iterative strategy, optimizing one tensor at a time while assuming all other tensors to be fixed. A sensible reason to choose this strategy is that the optimization problem for a single tensor $\Lambda^{[l,n]}$ actually reduces to a simple eigenvalue problem for an effective Hamiltonian $H^{[l,n]}_{\text{eff}}$ acting on the degrees of freedom of $\Lambda^{[l,n]}$ alone, in an analogous fashion to the density matrix RG with single center site[34]. To see this, we define iteratively for each virtual site $[l,n]$ the effective Hamiltonian terms $\mathcal{H}^{[l,n]}$, $\mathcal{H}^{\alpha[l,n]}_{\leftarrow}$ and $\mathcal{H}^{\alpha[l,n]}_{\rightarrow}$, resulting from performing the isometric mapping operation sketched in Fig. 4. By identifying the effective Hamiltonian terms on the physical sites layer as the original Hamiltonian, i.e. $\mathcal{H}^{[L,n]} \equiv \mathcal{H}^{[n]}$, $\mathcal{H}^{\alpha[L,n]}_{\leftrightarrow} \equiv \mathcal{H}^{\alpha[n]}_{\leftrightarrow}$ the

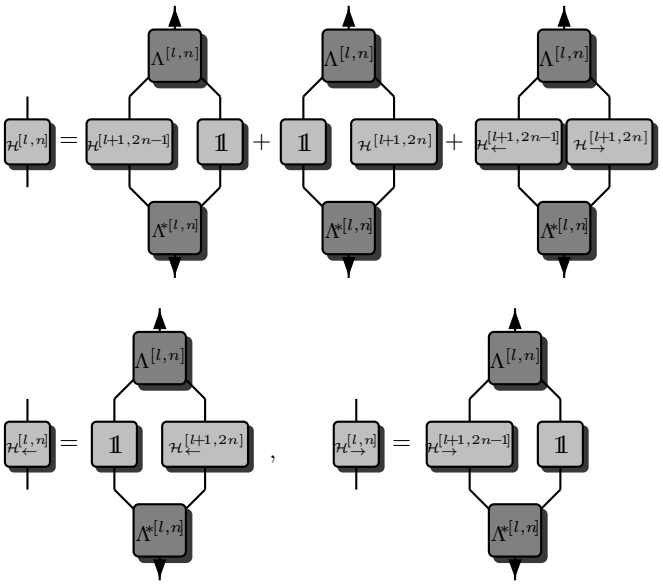

FIG. 4: Mapping operation induced by the tensor $\Lambda^{[l,n]}$. The operation maps the effective Hamiltonian terms at sites [l+1,2n-1] and [l+1, 2n] to the new terms at site $[l,n]$. The index α has been dropped for simplicity.

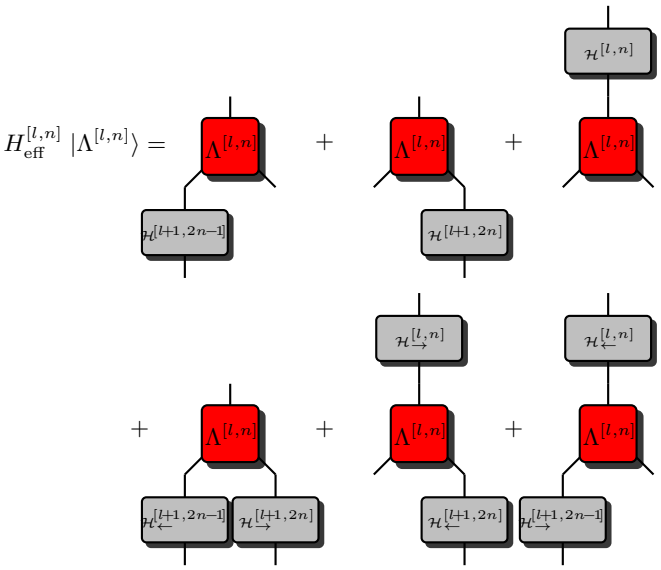

FIG. 5: Definition of the action of the effective Hamiltonian $H_{\text{eff}}^{[l,n]}$ on the degrees of freedom of the tensor $\Lambda^{[l,n]}$. (Again, the index α has been dropped for simplicity.)

mapping is a well-defined operation for every link. On the other hand, we do not have to explicitly define effective identity operators $\mathcal{N}^{[l,n]}$, since the identity operator $\mathbb{1}$ is invariant under the mapping by construction. The mapping is always to be carried in the direction of the adaptive gauge isometrization: starting from contracting the Hamiltonian pieces which are farther from the node $[l,n]$ in the network metric, and then proceeding closer and closer, until the effective Hamiltonian only acts on $\Lambda^{[l,n]}$ itself. According to this picture, the calculation of the energy expectation value for the TTN can be written down as $E = \langle\Lambda^{[l,n]}|H_{\text{eff}}^{[l,n]}|\Lambda^{[l,n]}\rangle$, where the action of $H_{\text{eff}}^{[l,n]}$ on $|\Lambda^{[l,n]}\rangle$ is meant as indicated in Fig. 5. The minimization problem for $\Lambda^{[l,n]}$, subject to the constraint of normalization, is then easily solved by the method of Lagrange multipliers. We then write the following Lagrangian

$$\mathcal{L}\left(|\Lambda^{[l,n]}\rangle, \langle\Lambda^{[l,n]}|, \lambda\right) = \langle\Lambda^{[l,n]}|H_{\text{eff}}^{[l,n]}|\Lambda^{[l,n]}\rangle - \lambda\left(\langle\Lambda^{[l,n]}|\mathbb{1}|\Lambda^{[l,n]}\rangle - 1\right) , \quad (3)$$

and since tensors different from $\Lambda^{[l,n]}$ are assumed to be fixed, the Euler-Lagrange equation simply reads

$$H_{\text{eff}}^{[l,n]}|\Lambda^{[l,n]}\rangle = \lambda\,\mathbb{1}|\Lambda^{[l,n]}\rangle , \quad \langle\Lambda^{[l,n]}|\mathbb{1}|\Lambda^{[l,n]}\rangle = 1 . \quad (4)$$

which is a *standard* eigenvalue problem (SEP) for $H_{\text{eff}}^{[l,n]}$. By linearity, it is readily seen that the normalized eigenvector of $H_{\text{eff}}^{[l,n]}$ corresponding to the lowest eigenvalue is the best choice for $\Lambda^{[l,n]}$ to minimize E. We highlighted on purpose the identity operators in Eq. (4), in order to stress the benefit that is obtained from the isometric gauge selection: In fact, choosing a different gauge would require to substitute the $\mathbb{1}$ for a (nontrivial) effective identity operator $\mathcal{N}^{[l,n]}$, turning Eq. (4) into a *generalized* eigenvalue problem, which is significantly more demanding and unstable than a SEP when addressed numerically[35].

After these considerations, the ground state search algorithm is summarized as follows:

(i) Initialize all tensor entries:

  (a) by picking a random state in the TTN manifold;

  (b) by selecting a particularly symmetric or meaningful state (e.g. a ferromagnetic product state);

  (c) by performing some iterations of an exponentially growing DMRG-like procedure;

  In the following, we focus on strategy (a) to prove that the algorithm is robust, as its convergence is ultimately insensitive to the initialization.

(ii) Select a tensor $\Lambda^{[l,n]}$ in the network. Isometrize the TTN in the direction of $\Lambda^{[l,n]}$ and perform the mapping operations according to the directed network. Optimize $\Lambda^{[l,n]}$ by solving Eq. (4).

(iii) From $\Lambda^{[l,n]}$ move to the next tensor $\Lambda^{[l',n']}$, adjusting the isometrization and updating the effective Hamiltonian terms. Note that only tensors located on the path connecting $\Lambda^{[l,n]}$ and $\Lambda^{[l',n']}$ are affected by this move (see Fig. 6). Having determined the new effective Hamiltonian, optimize $\Lambda^{[l',n']}$ via Eq. (4) again.

(iv) Repeat (iii), targeting each tensor in the tree by following some "sweeping" pattern (e.g. the one indicated in Fig. 6); stop when convergence in the

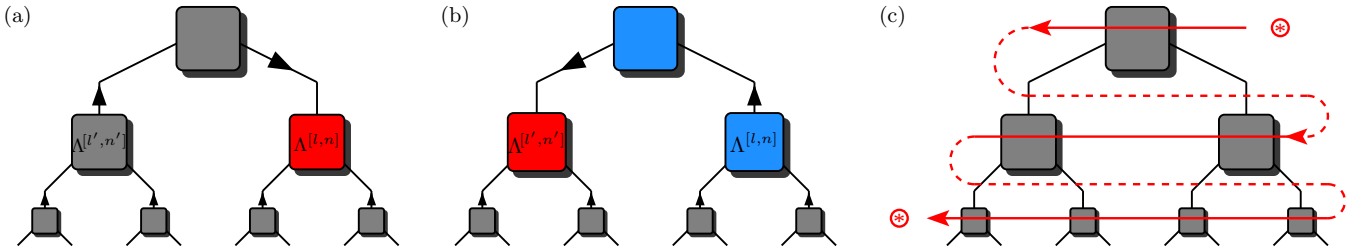

FIG. 6: Generic optimization move: (a) After optimizing $\Lambda^{[l,n]}$, the tensor $\Lambda^{[l',n']}$ is targeted for optimization. (b) Only tensors and effective Hamiltonian terms located on the path connecting $\Lambda^{[l,n]}$ and $\Lambda^{[l',n']}$ (colored in blue) need to be updated in order to enable the optimization of $\Lambda^{[l',n']}$. (c) Targeting each tensor in the tree multiple times results in a sweeping pattern. After completing a sweep, resume at the top (as indicated by the encircled marks).

ground state energy is reached, according to some precision threshold.

The sweeping action is the key point which pushes the TTN representation beyond the simple numerical real space RG-flow: Optimizing multiple times the same tensor while tuning the environment (i.e. the rest of the network surrounding it) makes the algorithm a complete variational approach, guaranteed to converge in the TTN manifold. Summing up, we have reduced the energy minimization problem to a sequence of QR-decompositions, linear mapping operations and SEPs, all of which can be carried out in a numerically stable fashion with a computational cost of $\mathcal{O}(m^4)$. Let us stress that this scaling behavior is independent of the boundary conditions chosen, at a difference with MPS ansätze; the only change accompanying a switch from PBC to OBC consists in omitting the terms that mediate the interaction between the physical sites 1 and N when calculating the action of the effective Hamiltonian (Fig. 5). These terms only occur for the outermost tensors in a layer (i.e. $n = 1$ or $n = 2^l$), and thus produce a subleading change in the overall computational cost. Moreover, we remark that the $\mathcal{O}(m^4)$ contraction cost relies only on the loop-free network structure and the fact that tensors have three legs: this means that the binary TTN ansatz can naturally be extended to other lattices and dimensionalities (e.g. 2D, Cayley trees[7]) without increasing the numerical effort for the contractions.

We conclude this section by describing how to extract expectation values of the TTN state $|\Psi\rangle$. This is particularly convenient for local observables $O^{[n]}$, having support on a single lattice site n. By isometrizing the TTN with respect to $\Lambda^{[L-1,\lceil n/2 \rceil]}$ (i.e. the tensor directly attached to site n; $\lceil x \rceil$ is the ceiling function of x), the expectation value $\langle\Psi|O^{[n]}|\Psi\rangle$ collapses to a contraction of only three tensors, as indicated in Fig. 7. In the case of two-point correlators $\langle O^{[n]}O^{[n+r]}\rangle$ (two local observables separated by a distance r) a similar procedure can be adopted; the only difference is that now nontrivial contractions arise for all tensors on the network path connecting the two sites n and $n + r$ (which is unique thanks to the loop-free network structure). Given that

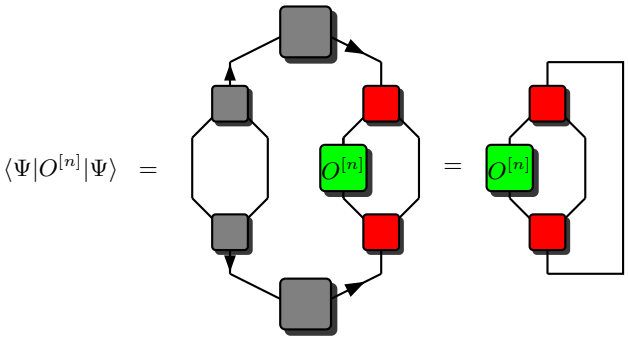

FIG. 7: Expectation value of a local observable $O^{[n]}$. Due to the isometry condition, the calculation always reduces to a contraction involving only three tensors.

the maximum number of tensors on this path scales logarithmically in the lattice size N, two-point correlators can be computed very efficiently.

III. TRANSLATIONAL INVARIANCE IN THE TTN ARCHITECTURE

Before benchmarking the presented algorithm, let us analyse the issue of the translational invariance of the lattice, which is broken by the design of the TTN ansatz. Indeed, it is clear from Fig. 1 that some sites are better connected with their immediate environment (i.e. the neighbouring sites) than others[36]. For instance, a very poorly connected environment occurs for the sites at $N/2$ and $N/2 + 1$, which are nearest neighbors, and yet they are renormalized together (in the RG-flow picture) only at the last step, i.e. at the very top of the tree network. The translational symmetry breaking induced by the TTN design makes one wonder what is the best strategy to obtain most accurate observation results when we are simulating a translationally invariant model. A legitimate question is whether it is beneficial or detrimental to measure at one site (or region) in particular rather than translationally averaging the measurements over the lattice. An analysis in this direction has been recently developed for a two-dimensional TTN design and reported

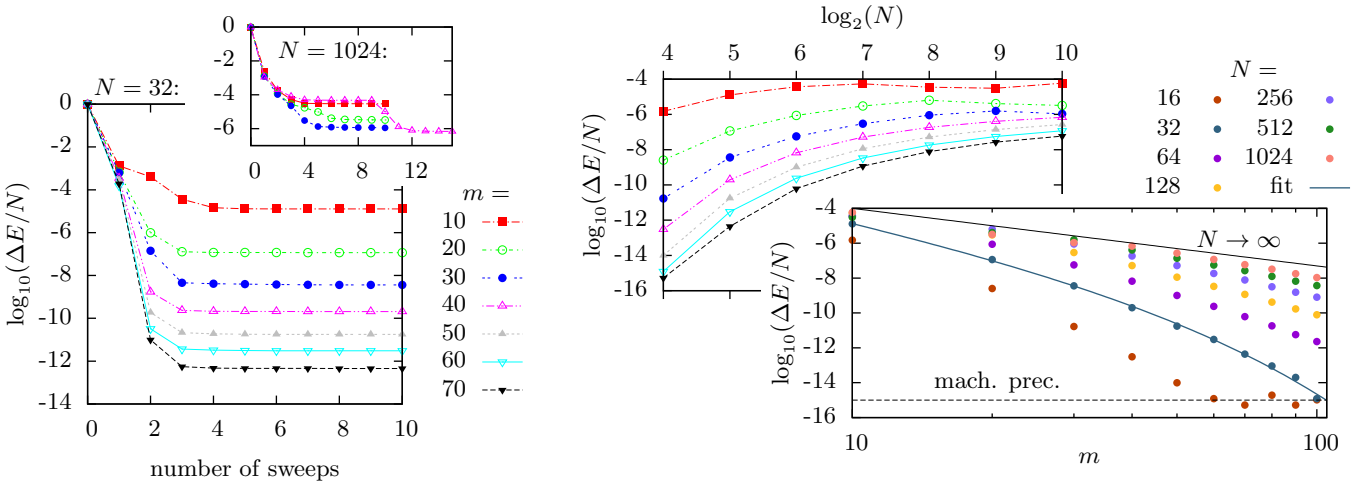

FIG. 8: Ising model: Error of the ground state energy per site $\Delta E/N$ as a function of the number of optimization sweeps for two different system sizes $N = 32$ and $N = 1024$ (left). Error as a function of the system size (right-upper). The same quantity as a function of the bond dimension m. The data for $N = 32$ is fitted by $a \cdot m^{-b} \cdot \exp(-c\,m)$, with $a = 12.8$, $b = 5.5$, $c = 0.11$. Extrapolation to the thermodynamic limit suggests a polynomial decay of the form $\Delta E \propto m^{-3.3}$ (right-lower).

in Ref. 36: in that scenario, a significantly more accurate description of local quantities has been obtained by focusing on "central sites", which are defined by the criterion that the Hilbert space of their immediate environment is largest. In our 1D setting we can identify the location s_c of these sites by alternately following the left (l) or right (r) branch down the tree, starting from the top, as indicated in the following sketch:

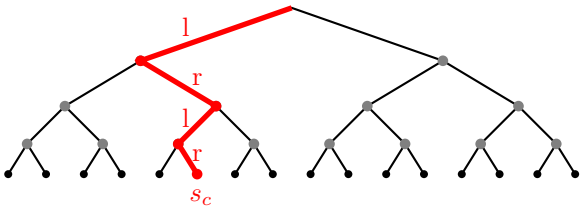

Algebraically, this can be written as

$$s_c = 1 + \sum_{l=1}^{\lfloor L/2 \rfloor} 2^{L-2l} = \lfloor (N+2)/3 \rfloor \,, \qquad (5)$$

where $\lfloor x \rfloor$ is the floor function of x. In order to clarify the situation for the 1D-TTN, we will use a benchmark Ising model to compute local observables and two-point correlators at all lattice sites and compare them with their respective system-wide averages. The results of this analysis will be presented at the end of the next section.

IV. BENCHMARKING OF THE ALGORITHM

To test the algorithm outlined in Sec. II we consider the spin-$\frac{1}{2}$ Ising model in a transverse field with PBC, defined by the Hamiltonian

$$H = -\sum_{n=1}^{\mathrm{PBC}} \sigma_n^x \sigma_{n+1}^x + h\,\sigma_n^z \,, \qquad (6)$$

where σ_n^α ($\alpha = x, y, z$) is a Pauli matrix acting on spin n and the parameter h is the external magnetic field. We will focus on the critical point of the model at $|h| = 1$, where, as previously stated and argued e.g. in Refs. 20,23,37, the entanglement scaling of TTN should prove more useful. This analytically solvable model[38,39] constitutes a commonly employed excellent benchmark for the quantities of our interest: namely, the ground state energy E, the central charge c, and the spin-correlation functions $C^\alpha(r) = \langle \sigma_n^\alpha \sigma_{n+r}^\alpha \rangle - \langle \sigma_n^\alpha \rangle \langle \sigma_{n+r}^\alpha \rangle$ including their respective critical exponents η_α.

First of all we report the convergence behavior of the algorithm, shown on the left hand side of Fig. 8: Convergence to the ground state as a function of the number of optimization sweeps is fast, with roughly fifteen sweeps being sufficient to reliably achieve the global minimum in the TTN state space, even for big system sizes of $N = 1024$ sites. As can be seen from the upper right plot in Fig. 8, the error of the ground state energy per site tends to be size-independent with increasing N, a feature the TTN shares with other hierarchical tensor network ansätze[28], when simulating a (1+1)D gapless system. An intuitive argument to motivate this is that, in order to describe the entanglement of a localized region with given precision, one has to pick a fixed value m and not one that scales with the length L: in a critical scenario, this can happen only if a given m captures the critical correlation scaling, i.e. the logarithmic entanglement area law violation. In the lower right graph we plot the dependency of the error on the bond dimension m. In double-logarithmic representation the curves clearly exhibit a negative curvature, meaning that the decay is sub-polynomial for any finite N; in the relevant range of m the behavior can be described well by a combined polynomial-exponential decay of the form $\Delta E(m) = a \cdot m^{-b} \cdot \exp(-c\,m)$, where a, b, c are fit

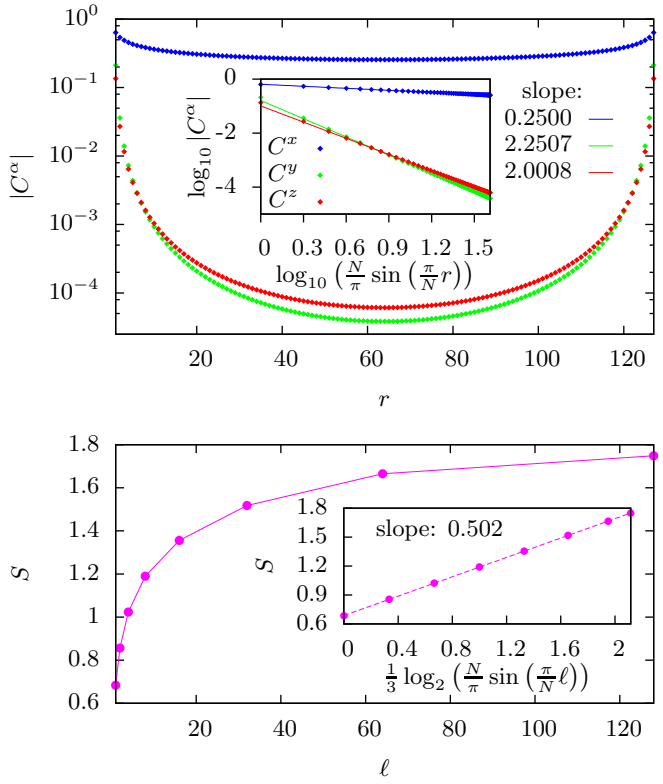

FIG. 9: (Top) Spin-correlation functions and fitted critical exponents, for a PBC quantum Ising chain of $N = 128$ sites, bond dimension $m = 100$. The exact exponents are $\eta_x = 0.25$, $\eta_y = 2.25$, $\eta_z = 2$. In order to account for the TTN-induced translational symmetry breaking, the correlations of distance r are obtained by averaging over lattice locations within branches wide enough to span r (see text). (Bottom) Von Neumann entropy of a $N = 256$ ($m = 100$) chain, for partitions of length ℓ and with fitted central charge. The exact central charge is $c = 0.5$.

parameters dependent on the system size (see Fig. 8). In the thermodynamic limit $N \to \infty$ the decay seems to be governed by a polynomial behavior of the form $\Delta E(m) \propto m^{-3.3}$.

In order to assess how the TTN deals with criticality and, consequently, strongly correlated systems, we report the spin-correlation functions and the von Neumann entropy in Fig. 9. Since we are at criticality, we expect the correlation functions to decay according to a power law $C^\alpha(r) \propto [\mathrm{crd}(r)]^{-\eta_\alpha}$, where $\mathrm{crd}(r) \equiv N/\pi \cdot \sin(\pi r/N)$ is the chord function giving the effective distance of two sites at distance r arranged on a ring of N sites[25,40,41]. The critical exponents are analytically known[41] to be $\eta_x = 1/4$, $\eta_y = 9/4$, and $\eta_z = 2$. The via fitting numerically obtained exponents in the upper panel of Fig. 9 show an agreement of the order of $\mathcal{O}(10^{-4})$, presenting state-of-the-art accuracy to the best of our knowledge[28]. The von Neumann entropy $S(\ell) \equiv -\mathrm{Tr}[\rho_\ell \ln \rho_\ell]$ of a partition of ℓ sites for PBC critical (1+1)D systems is known to behave according to $S(\ell) = c/3 \cdot \log_2[\mathrm{crd}(\ell)] + \mathrm{const.}$, where c is the central charge of the underlying conformal field theory [42], and for the Ising model we have $c = 1/2$. Again, we have very good agreement of the exact value with the numerically determined central charge $c = 0.502$ shown in the lower panel of Fig. 9, proving that the TTN ansatz is well suited for reproducing a system at criticality. In particular, we showed that even with a relatively small bond dimension m, it is perfectly meaningful to simulate critical systems even with hundreds of sites, and indeed achieve a high precision of the results.

We conclude this section by addressing the question raised in Sec. III, i.e. whether or not it is beneficial to average over expectation values. For this purpose we compute the local energy $E_n = -\langle\sigma^x_n\sigma^x_{n+1}\rangle + \langle\sigma^z_n\rangle$ for the critical Ising model Eq. (6) and plot the absolute value of its error ΔE_n as a function of the site location (see Fig. 10). Also shown is the error of the system-wide average $\sum_{n=1}^N E_n/N$. It is clear from Fig. 10 that the averaged quantity is about one order of magnitude more accurate than the vast majority of the individual measurements (including the location of the central sites s_c as defined in Eq. (5)). This is due to the fact that the E_n are scattered above and below the exact value, resulting in an average that is more accurate. Although isolated sites more accurate than the average value exist, these do not occur at specific locations independent of m, which is why this behavior has to be attributed to numerical fluctuations rather than to some systematic reason. Therefore, Fig. 10 strongly suggests that averaging over all sites is the best way to extract local observables from a 1D-TTN. We proceed to analyze the averaging issue for correlation functions. Since it is efficient to calculate correlators $C^\alpha_{n,n+r}$ for every distance r and pair position n, we can easily address the question whether or not it is profitable to calculate the average $\sum_{n=1}^N C^\alpha_{n,n+r}/N$ for a given pairwise distance r. Fig. 10 shows the error $\Delta C^y_{n,n+r}$ of the spin correlations in y-direction as a function of n and r. Immediately noticeable is a triangular pattern, indicating that with increasing r the accuracy abruptly degrades each time a major branch in the tree is trespassed. The zoomed panels show that for this reason it is advantageous (especially for short distances), to measure the correlator within a branch wide enough to span the given distance, i.e. within the dark blue areas of figure Fig. 10. Averaging, in this case, is mainly detrimental and results in significantly bigger errors, up to two orders of magnitude.

V. BILINEAR-BIQUADRATIC SPIN-1 CHAIN

After having benchmarked the adaptive TTN algorithm on the spin-1/2 quantum Ising model, in this section we turn to a numerically very challenging transition in $SU(2)$ invariant spin-1 chains. We consider indeed the

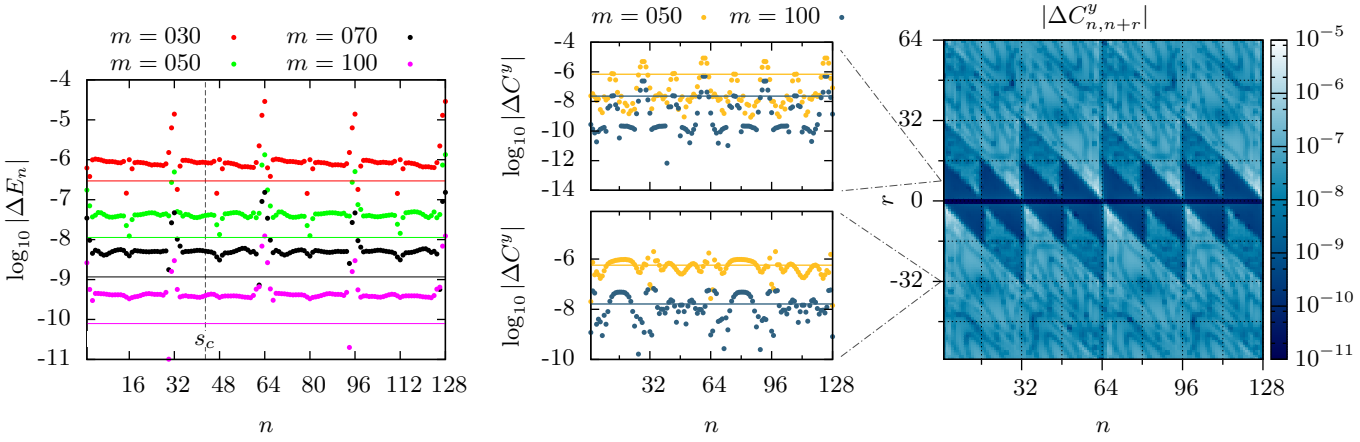

FIG. 10: Error of the local energy E_n as a function of the lattice site n for different bond dimensions m, in the critical quantum Ising model with PBC defined in Eq. (6). The solid lines are the errors of the system-wide averages. The vertical dashed line indicates the location of the center site s_c (left). Error of the spin two-point correlator $C^y_{n,n+r}$ for bond dimension $m = 100$ (right); the two insets show the data at fixed distance r together with system-wide averages for $r = 8$ (top) and $r = -32$ (bottom).

bilinear-biquadratic Hamiltonian ($H \equiv \sum_{n=1}^{N-1} h_{n,n+1}$):

$$H = \sum_{n=1}^{N-1} \cos\theta \left(\vec{S}_n \cdot \vec{S}_{n+1}\right) + \sin\theta \left(\vec{S}_n \cdot \vec{S}_{n+1}\right)^2 , \quad (7)$$

whose phase diagram[43,44] is provided in Fig. 11 as a function of the parameterizing angle θ. While most phase boundaries have been set on firm grounds relatively early[45–49], the region between the translationally broken dimer and the rotationally broken ferromagnet have been subject of a long and controversial debate[44,49–57]. An intermediate nematic phase, restoring the translational invariance while mildly breaking the rotational one by a quadrupolar moment, has been conjectured[50,51] in the range $-3\pi/4 \equiv \theta_F \leq \theta \leq \theta_C \simeq -0.67\pi$. The competing order parameters would then be: the dimerization D[48]

$$D_n = |\langle h_{n-1,n} - h_{n,n+1} \rangle| , \quad (8)$$

which can be non-zero in 1D finite chains; and a quadrupole moment Q_Ω (with $\vec{e}_\Omega$ a unit vector pointing to the solid angle Ω)

$$Q_{n,\Omega} = (\vec{S}_n \cdot \vec{e}_\Omega)^2 - 2/3 , \quad (9)$$

of which only quasi-long range order in correlations can be measured in 1D finite chains (see Eq. (12)). Increasingly powerful numerical techniques[44,49,52–57] and improved theoretical analyses[59–61] have shrunk more and more the nematic window, by accumulating evidences of an exponentially vanishing D accompanied by an exponentially growing quadrupole correlation length ξ_Q. The latter accounts for the extreme difficulty in ruling out a quasi-long range nematic order only based on numerical data of finite-size chains. A recent description of the Berry phases of quantum fluctuations[59] predicted the following scalings with $\Delta\theta = \theta - \theta_F$:

$$D \approx \exp\left(-\pi^2/(8\Delta\theta)\right) , \quad (10a)$$

$$\xi_Q \approx \exp\left(\pi\sqrt{2/\Delta\theta}\right) . \quad (10b)$$

The data we obtain from our adaptive TTN procedure actually nicely agree with this prediction, as we argue below, and thus corroborate the validity of the presented method also in non-trivial cases.

First, we assess the numerical precision of the adaptive TTN algorithm by analysing its performances in the purely biquadratic Klümper point[58] at $\theta = \theta_K = -\pi/2$ (empty circle in Fig. 11). The ground state energy in the thermodynamic limit can be analytically obtained by Bethe Ansatz (after a mapping to a spin-1/2 XXZ chain)

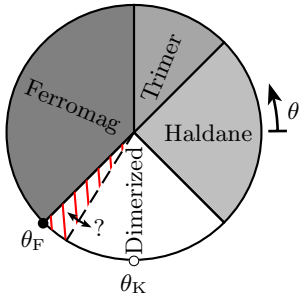

FIG. 11: Phase diagram of the bilinear-biquadratic model of Eq. (7), with four firmly established phases: ferromagnetic, trimerized[49], Haldane antiferromagnet[45,46] and dimerized[47,48]. According to the most recent studies and the data obtained here with adaptive TTN, no intermediate nematic phase (originally hypothesized location indicated by red hatched region[50,51]) is emerging around θ_F (black dot). The white dot identifies the Klümper point[47,58] whose Bethe ansatz solution in Eq. (11) we use to benchmark the numerical precision of our algorithm.

as[47,62]

$$E/N = -1 - 2\sqrt{5}\left(\frac{1}{4} + \sum_{k=1}^{\infty} \frac{1}{1+\left[\left(3+\sqrt{5}\right)/2\right]^{2k}}\right) = -2.79686343\ldots, \quad (11)$$

and will serve as a reference for our finite-bond and finite-size extrapolation procedure. This consists in taking first the limit $m \to \infty$ for every chain length N (according to the empirical formula indicated in Fig. 8), as illustrated in the inset of Fig. 12, and then considering the thermodynamic limit $N \to \infty$ by a linear fit in $1/N$ to eliminate edge effects, as shown in the main plot of Fig. 12. The thus estimated energy $E_{\mathrm{TTN}} = -2.79670(1)$ has a precision of 10^{-4}.

We then proceed to evaluate, for various values of $\theta \in [\theta_{\mathrm{F}}, \theta_{\mathrm{K}}]$, the dimerization D of Eq. (8). In order to avoid issues related to resonant superpositions of different dimerized configurations, we resort to open boundary conditions. We avoid end effects of the open chain by measuring the dimerization only at sites that are sufficiently far away from the edges. The data presented in the upper plot of Fig. 13 nicely agree with the prediction of Eq. (10a), displaying a clear exponential behavior in $1/\Delta\theta$.

Finally, we proceed to compute the correlation of quadrupole moments at a long distance r averaged over the solid angle:

$$\begin{aligned} C^{\mathrm{Q}}(r) &= \int \frac{\mathrm{d}\Omega}{4\pi} \langle Q_{n,\Omega}\, Q_{n+r,\Omega}\rangle - \langle Q_{n,\Omega}\rangle\langle Q_{n+r,\Omega}\rangle \quad (12)\\ &= \frac{2}{15}\sum_{\alpha} \left\langle \left(S_n^{\alpha}\right)^2 \left(S_{n+r}^{\alpha}\right)^2 \right\rangle - \left\langle \left(S_n^{\alpha}\right)^2 \right\rangle \left\langle \left(S_{n+r}^{\alpha}\right)^2 \right\rangle \\ &+ \frac{1}{15}\sum_{\alpha<\beta} \left\langle T_n^{\alpha\beta} T_{n+r}^{\alpha\beta} \right\rangle - \left\langle T_n^{\alpha\beta} \right\rangle \left\langle T_{n+r}^{\alpha\beta} \right\rangle , \end{aligned}$$

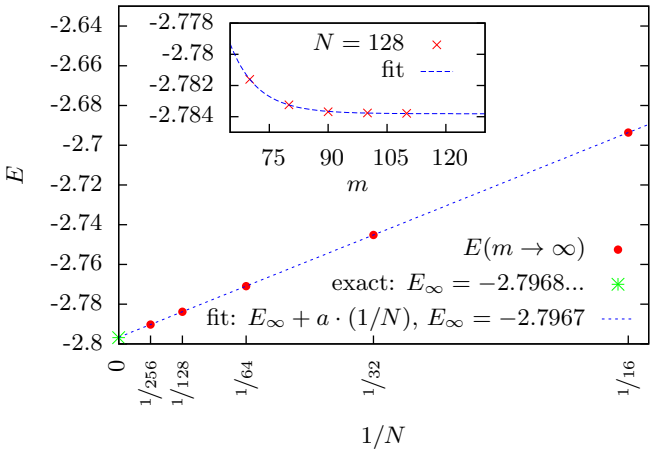

FIG. 12: Extrapolation to the thermodynamic limit of the ground state energy at the purely biquadratic point $\theta = -\pi/2$. The inset shows the extrapolation in the bond dimension for $N = 128$, using a fit similar to the one indicated in Fig. 8.

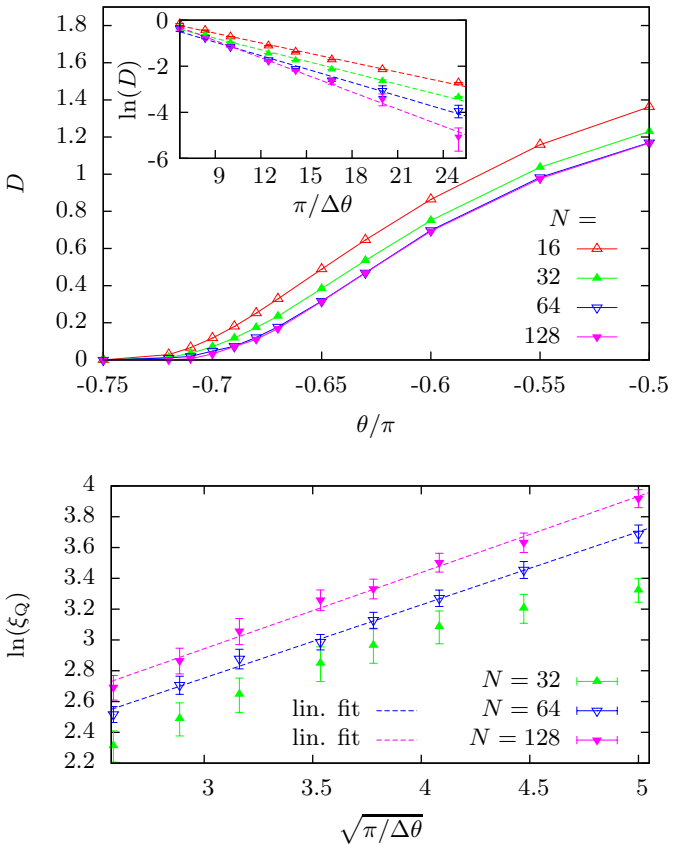

FIG. 13: (Top) Dimerization parameter D for various system sizes. Each data point is the result of an extrapolation $m \to \infty$ in the bond dimension. The dashed lines shown in the inset are linear fits. (Bottom) Quadrupolar correlation length ξ_{Q}, obtained from fitting the correlation function Eq. (12). Each $C^{\mathrm{Q}}(r)$ has been extrapolated to $m \to \infty$ (for every r) before the correlation length was extracted. Reported error bars are fit errors. The large error bars for $N = 32$ are caused by the fact that the chain is too small to contain meaningful information on the long-range property ξ_{Q}.

with the anticommutator $T_n^{\alpha\beta} \equiv \{S_n^{\alpha}, S_n^{\beta}\}$. The correlation length ξ_{Q} is then extracted by fitting the $m \to \infty$ extrapolations with $C^{\mathrm{Q}}(r) = a\, r^{-\eta} \exp(-r/\xi_{\mathrm{Q}})$, where a is a prefactor and η is an exponent. The results are shown in the lower panel of Fig. 13 and provide quite clear evidence of an exponential growth of ξ_{Q} with $1/\sqrt{\Delta\theta}$. In summary, these results support Eqs. (10) and therefore indicate the non-existence of the nematic phase.

VI. CONCLUSIONS

In this manuscript we introduced, motivated, and discussed an algorithm for simulating ground states of quantum many-body Hamiltonians on a lattice, based on a gauge-adaptive tree tensor network ansatz. We stressed how the manipulation at runtime of the tensor network

gauge, combined with the loop-free topology of the tree network, plays an instrumental role in enhancing the performance of the algorithm, first of all, by reducing a generalized eigenvalue problem into a simple eigenvalue problem. We characterized the computational scalings with bond dimension m and argued how the algorithm speed-up allows for pushing to higher numerical precision. We tested the algorithm on 1D quantum models, with various boundary conditions: first we benchmarked it against the exactly solvable Ising model in a transverse field, extracting very precise critical exponents with PBC's; then we explored the bilinear-biquadratic spin-1 model in a region known to be numerically challenging, being able to confirm an intricate exponential explosion of (nematic) correlation lengths towards the transition point. Moreover, we investigated how well the TTN ansatz can restore the broken translational invariance in 1D, and verified that while for local quantities averaging over translations is a winning strategy, for correlation functions evaluating over highly-entangled clusters is a more suitable approach.

The redirectionable isometric gauge presented here allows also for a convenient, natural treatment of preserved global symmetries, both abelian and non-abelian, which result in a block-diagonal structure of the tensor entries with clear, unique selection rules and structure constants[63–65] (in this framework, a simultaneous double-tensor optimization scheme would help circumventing the related intermediate charge-targeting issues[34]). Similarly, lattice gauge symmetries, which in contrast to global symmetries act on local compact supports of the 1D chain of sites, can be rigorously and efficiently cast in tensor network language[66–69], and in particular in a TTN ansatz.

An additional research direction is offered by the recently introduced time dependent variational principle for tensor network states[70], whose purpose is to describe efficiently out-of-equilibrium dynamics: indeed it can be elegantly and successfully tailored to TTN, free of tensor gauge complications thanks to the loop-free geometry of the tree network.

Finally, we stress again that the flexibility of the gauge-adaptive TTN ansatz presented here, and especially the fact that its scaling is independent from the specific (open or periodic) boundary conditions, makes it an extremely promising tool to attack and solve open complex many-body problems spanning from condensed matter to quantum information. Moreover, the presented approach can be trivially extended to include lattice dimensions higher than one with the same polynomial scaling of the algorithms computational cost.

ACKNOWLEDGEMENTS - We thankfully acknowledge J.I. Cirac for inspiring this work, for feedback and discussions. Authors acknowledge financial support from EU through SIQS, the German Research Foundation (DFG) via the SFB/TRR21, Italian MIUR via PRIN Project 2010LLKJBX, and computational resources provided by the bwUniCluster and bwGRiD projects in Ulm and by the MOGON cluster of the ZDV Data Center in Mainz.

[1] F. Verstraete, D. Porras, and J. Cirac, Phys. Rev. Lett. **93**, 4 (2004), ISSN 1079-7114.
[2] G. Vidal, Phys. Rev. Lett. **91**, 147902 (2003).
[3] D. Perez-Garcia, F. Verstraete, M. M. Wolf, and J. I. Cirac, Quantum Inf. Comput. **7**, 401 (2007).
[4] U. Schollwöck, Ann. Phys. **326**, 96 (2011).
[5] G. D. Chiara, M. Rizzi, D. Rossini, and S. Montangero, J. Comput. Theor. Nanosci. **5**, 1277 (2008).
[6] S. R. White, Phys. Rev. Lett. **69**, 2863 (1992).
[7] V. Murg, F. Verstraete, O. Legeza, and R. M. Noack, Phys. Rev. B **82**, 205105 (2010).
[8] K. H. Marti, B. Bauer, M. Reiher, M. Troyer, and F. Verstraete, New J. Phys. **12**, 103008 (2010).
[9] G. Vidal, J. I. Latorre, E. Rico, and A. Kitaev, Phys. Rev. Lett. **90**, 227902 (2003).
[10] J. I. Latorre, E. Rico, and G. Vidal, Quant. Inf. Comput. **4**, 48 (2004).
[11] F. Verstraete and J. I. Cirac, Phys. Rev. B **73**, 094423 (2006).
[12] J. Eisert, M. Cramer, and M. Plenio, Rev. Mod. Phys. **82**, 277 (2010).
[13] T. Barthel, M. Kliesch, and J. Eisert, Phys. Rev. Lett. **105**, 010502 (2010).
[14] G. Evenbly and G. Vidal (2013), arXiv:1310.8372 [quant-ph].
[15] F. Verstraete, M. M. Wolf, D. Perez-Garcia, and J. I. Cirac, Phys. Rev. Lett. **96**, 220601 (2006).
[16] K. H. Mart, B. Bauer, M. Reiher, M. Troyer, and F. Verstraete, New J. Phys. **12**, 103008 (2010).
[17] J. Molina, JHEP **5**, 024 (2013).
[18] K. G. Wilson, Rev. Mod. Phys. **47**, 773 (1975).
[19] Y.-Y. Shi, L.-M. Duan, and G. Vidal, Phys. Rev. A **74**, 022320 (2006).
[20] P. Silvi, V. Giovannetti, S. Montangero, M. Rizzi, J. I. Cirac, and R. Fazio, Phys. Rev. A **81**, 062335 (2010).
[21] G. Vidal, Phys. Rev. Lett. **99**, 220405 (2007).
[22] M. Rizzi, S. Montangero, and G. Vidal, Phys. Rev. A **77**, 052328 (2008).
[23] V. Giovannetti, S. Montangero, and R. Fazio, Phys. Rev. Lett. **101**, 180503 (2008).
[24] G. Evenbly and G. Vidal, J. Stat. Phys. **145**, 891 (2011).
[25] G. Mussardo, *Statistical Field Theory*, Oxford university press (2009).
[26] J. Cardy, J. Phys. A **42**, 504005 (2009).
[27] L. Tagliacozzo, G. Evenbly, and G. Vidal, Phys. Rev. B **80**, 235127 (2009).
[28] G. Evenbly and G. Vidal, Phys. Rev. B **79**, 144108 (2009).
[29] M. Aguado and G. Vidal, Phys. Rev. Lett. **100**, 070404 (2008).
[30] C. D. Batista and G. Ortiz, Phys. Rev. Lett. **86**, 1082 (2001).
[31] L. Wang, I. Pižorn, and F. Verstraete, Phys. Rev. B **83**,

134421 (2011).
[32] A. J. Ferris and G. Vidal, Phys. Rev. B **85**, 165146 (2012).
[33] R. A. Horn and C. R. Johnson, *Matrix Analysis* (Cambridge University Press, 2012), ISBN 0521839408.
[34] S. R. White, Phys. Rev. B **72**, 180403 (2005).
[35] Z. Bai, J. Demmel, J. Dongarra, A. Ruhe, and H. van der Vorst, *Templates for the solution of algebraic eigenvalue problems: a practical guide*, vol. 11 (Siam, 2000), ISBN 0898714710.
[36] A. J. Ferris, Phys. Rev. B **87**, 125139 (2013).
[37] G. Vidal, Phys. Rev. Lett. **101**, 110501 (2008).
[38] E. Lieb, T. Schultz, and D. Mattis, Annals of Physics **16**, 407 (1961).
[39] P. Pfeuty, Annals of Physics **57**, 79 (1970).
[40] M. A. Cazalilla, J. Phys. B **37**, S1 (2004).
[41] S. Sachdev, *Quantum Phase Transitions* (Cambridge University Press, 2011).
[42] P. Calabrese and J. Cardy, Journal of Statistical Mechanics: Theory and Experiment **2004**, P06002 (2004).
[43] N. Papanicolaou, Nuclear Physics B **305**, 367 (1988).
[44] G. Fáth and J. Sólyom, Phys. Rev. B **51**, 3620 (1995).
[45] F. D. M. Haldane, Physics Letters A **93**, 464 (1983).
[46] F. D. M. Haldane, Phys. Rev. Lett. **50**, 1153 (1983).
[47] M. Barber and M. Batchelor, Phys. Rev. B **40**, 4621 (1989).
[48] Y. Xian, Physics Letters A **183**, 437 (1993).
[49] A. Läuchli, G. Schmid, and S. Trebst, Phys. Rev. B **74**, 144426 (2006).
[50] A. V. Chubukov, J. Phys.: Condens. Matter **2**, 1593 (1990).
[51] A. Chubukov, Phys. Rev. B **43**, 3337 (1991).
[52] N. Kawashima, Prog. Theor. Phys. Suppl. **145**, 138 (2002).
[53] B. A. Ivanov and A. K. Kolezhuk, Phys. Rev. B **68**, 052401 (2003).
[54] K. Buchta, G. Fáth, Ö. Legeza, and J. Sólyom, Phys. Rev. B **72**, 054433 (2005).
[55] M. Rizzi, D. Rossini, G. de Chiara, S. Montangero, and R. Fazio, Phys. Rev. Lett. **95**, 240404 (2005).
[56] D. Porras, F. Verstraete, and J. I. Cirac, Phys. Rev. B **73**, 014410 (2006).
[57] R. Orús, T.-C. Wei, and H.-H. Tu, Phys. Rev. B **84**, 064409 (2011).
[58] A. Klümper, EPL **9**, 8 (1989).
[59] S. Hu, A. M. Turner, K. Penc, and F. Pollmann (2014), arXiv:1401.3246 [cond-mat.str-el].
[60] R. Moessner, S. L. Sondhi, and E. Fradkin, Phys. Rev. B **65**, 024504 (2001).
[61] T. Grover and T. Senthil, Phys. Rev. Lett. **98**, 247202 (2007).
[62] E. Sørensen and A. Young, Phys. Rev. B **42**, 754 (1990).
[63] S. Singh, R. N. C. Pfeifer, and G. Vidal, Phys. Rev. A **82**, 050301 (2010).
[64] A. Weichselbaum, Ann. Phys. **327**, 2972 (2012).
[65] P. Silvi (2012), arXiv:1205.4198 [quant-ph].
[66] E. Rico, T. Pichler, M. Dalmonte, P. Zoller, and S. Montangero, Phys. Rev. Lett. **112**, 201601 (2014).
[67] B. Buyens, J. Haegeman, K. Van Acoleyen, H. Verschelde, and F. Verstraete (2013), arXiv:1312.6654 [hep-lat].
[68] P. Silvi, E. Rico, T. Calarco, and S. Montangero (2014), arXiv:1404.7439 [quant-ph].
[69] L. Tagliacozzo, A. Celi, and M. Lewenstein (2014), arXiv:1405.4811 [cond-mat.str-el].
[70] J. Haegeman, J. I. Cirac, T. J. Osborne, I. Pižorn, H. Verschelde, and F. Verstraete, Phys. Rev. Lett. **107**, 070601 (2011).